



# Heat transfer in aluminum-steel joint and weld tool during the friction stir welding: Simulation and experimental validation

Wenmin Ou<sup>1</sup> · Guolin Guo<sup>1</sup> · Chenshuo Cui<sup>1</sup> · Yaocheng Zhang<sup>1</sup> · Longgen Qian<sup>2</sup>

Received: 3 June 2022 / Accepted: 12 January 2023 / Published online: 19 January 2023  
© The Author(s), under exclusive licence to Springer-Verlag London Ltd., part of Springer Nature 2023

## Abstract

In this work, dissimilar butt joints of 6061 aluminum and 304 stainless steel were prepared by friction stir welding (FSW), and the FSW process is monitored by the infrared (IR) thermography. Considering the different material properties between aluminum and steel, a novel CFD model with weld tool is developed and tested to investigate the effects of weld tool on the aluminum-steel joint under different traverse speeds. The calculated temperature and thermal cycles for various traverse speed agreed well with the corresponding IR thermography experimental results. It is found that the calculated peak temperature is about 10 K lower than measured peak temperature and the relative error is 2.3%, while it is 11.4% for the model without weld tool. The model with weld tool can decrease the temperature gradient and inhomogeneity of temperature field for aluminum-steel joint. SEM analysis of the interface between aluminum and steel showed that the thickness of IMCs may decrease with traverse speed. The model with weld tool can provide calculated viscosity based on the validated temperature field to analyze the insufficient stirring defect of aluminum-steel joint.

**Keywords** Heat transfer behavior · Friction stir welding · Aluminum-steel joint · CFD model with weld tool · Infrared thermography observation

## 1 Introduction

Aluminum-steel composite structure can meet the industrial requirements of structural performance and lightweight design [1]. Therefore, joining of aluminum to steel is of increasing interest for a wide range of industrial applications [2]. The heat transfer controls aluminum-steel joint performance. If joining method is fusion weld, the peak temperature exceeds the melting point, so brittle intermetallic compounds (IMCs) are formed resulting in poor joint performance [3]. Friction stir welding (FSW) is solid state joining method which indicated the peak temperature is much lower than the melting point, so it can restrict the generation of IMCs [2]. Bagheri et al. [4] invented an advanced version of friction stir brazing (FSB) entitled friction stir vibration brazing (FSVB) to decrease the thickness of the IMC layer

and void volume percentage of low carbon steels. They also improved FSVB by investigating the effects of mechanical vibration and rotational speed on the temperature, the thickness of intermetallic compounds (IMCs) layers, and void volume percentage at the joint interface [5]. It is found that the interfacial IMCs layers thickness decreases as rotational speed increases from 850 to 1150 rpm. Bozzi et al. [6] investigated the interface Al 6016/IF-steel in friction stir welding spots, it is found that the thickness of IMCs layer can be restricted by decreasing heat flux in tool pin. Wan et al. [7] reviewed friction stir welding (FSW) of dissimilar aluminum alloys and steels, it is generally believed that the thickness of IMCs layer increases with the increase of heat input during the FSW process. Derazkola et al. [8] verified the Arrhenius relations between the thickness of the IMCs layer and the temperature in the butt joints of AA5005-O aluminum-magnesium alloy and St-52 low carbon steel sheets.

Thickness of IMCs layer is depended on the heat transfer during FSW. In order to control the heat transfer to obtain sound joints, special tools are designed including cutting pin with rotary burrs [9], tool with scribe made of tungsten carbide-cobalt cermet [10], and scrolled tool with scribe affixed to pin tip [11], etc. However, large differences in

✉ Wenmin Ou  
ouwenmin@csig.edu.cn

<sup>1</sup> School of Automotive Engineering, Changshu Institute of Technology, Changshu 215500, China

<sup>2</sup> School of Mechanical Engineering, Changshu Institute of Technology, Changshu 215500, China

their thermal properties such as expansion coefficient, conductivity, and specific heat can lead to defect. Understanding the effects of weld tool on the heat transfer behaviors in friction stir welding is of great significance for producing free defect joints based on scientific principles. But heat transfer behaviors with weld tool are difficultly measured because of the interaction between thermal and machinal and the complex profile between the tool and workpiece. As a result, the numerical analysis has been generally employed in investigating the effects of the welding tool on heat transfer behavior [12, 13].

It is more precise but more difficult to couple the weld tool into FSW numerical model. Su et al. [14] established a 3D full coupled CFD model with two tools of different pin shapes (axisymmetrical conical tool and asymmetrical triflat tool). In order to obtain higher precise in their model, the boundary conditions of heat transfer and material flow are determined with considering a partial sticking/sliding contact condition at the tool–workpiece interface. Bagheri et al. [15] expanded a numerical model with weld tool, corresponding to smoothed particle hydrodynamics, to consider the importance of vibration on temperature history, heat generation, stress distribution, and strain rate during the friction stir welding (FSW) process. In addition, the cooling influence, the effect of traveling speed, friction coefficient, mesh size, and the mass scaling technique to find the converged model and decrease the CPU time were also studied [16]. Sun et al. [17] developed a numerical model with weld tool to analyze the influence of tool thread pitch on the material flow and thermal process in FSW. Their results shows that the total heat generation decreases with thread pitch, which may not be measured in experiments. Chen et al. [18] also investigated the influent of pin thread on material flow and thermal process. Comparing with Sun’s model, their model is more complicated, in which the transient rotation of the threaded pin is implemented explicitly via fully transient control of the zone motion. Chen et al. [19] further compared the boundary velocity (BV) model and the boundary shear stress (BSS) model to analyze the heat transfer and plastic deformation behaviors during the FSW of AA2024. It was indicated that different boundary conditions yield similar predictions on temperature, but quite different predictions on deformation. The coupled thermomechanical FSW model [20, 21] and retractable pin tool model [22] provide detail technical information about setting boundary conditions and calculation zones, but they did not provide detail information about heat transfer in weld tool. It was generally noted that heat transfer between the welding tool and the workpiece can be applied to predict the heat generation and recrystallized grain. Aziz et al. [23] investigated the heat generation by considering heat transfer in weld tool. The simulation results showed that the highest relative error is below 6% by comparing simulated temperature profile of three different

weld schedules. Miles et al. [24] reported more precise result to predict recrystallized grain by considering heat transfer in weld tool. It also showed that the heat generated during FSW was predicted to within 5% of the experiment. Mirabzadeh et al. [25] developed a 3-D symmetric Finite Element (FE) model to estimate the generated and distributed heat for polypropylene sheet joints. It indicated that if the heat transfer in weld tool is well predicted, the number of experiment tests may be reduced.

In a summary, the model with weld tool is only tested for the same material joints. The underlying heat transfer and material flow mechanism of the coupling interaction between weld tool and workpiece for aluminum-steel joints is not yet clear. In this paper, there dimension model with weld tool is developed to calculate the heat transfer and material flow of aluminum-steel joint based on CFD. Since the FSW system is consists of aluminum, steel, weld tool head, and weld tool pin, the calculation zone is also divided into four parts. The boundary conditions are carefully set, especially at the tool/workpiece interface. The simulation results are validated by conducting infrared (IR) thermography experiments and optical microscopy (OM) experiments at different traverse speed. The effects of tool on heat transfer in the friction stir welding of aluminum-steel joint are discussed.

## 2 Experiment

Bead-on-plate friction stir welding was performed on 6061 aluminum alloy and 304 stainless steel in this study. The dimensions of each workpiece were 150 mm × 75 mm × 3 mm (length × width × thickness). The welding tool was made of the H13 steel. The welding tool shoulder was 18 mm in diameter, and length of the pin was 2.7 mm. The pin had a conical geometry. The diameter of pin was 7 mm near the shoulder and 5 mm at the tip.

A schematic view of the FSW system is illustrated in Fig. 1. Two kinds of IR cameras are used in the system, one is Optris PI-20072263 with measured temperature range from 293 to 1173 K, the other is Optris PI-20032134 with measured temperature range from 723 to 2073 K. The FSW equipment is developed from Computerized Numerical Control (CNC) machine tool. The 3 axis independent movements of the machine tool are programed and controlled by a software-based control system. The employed plunge depth was 0 mm, and no tilt angle was adopted. The steel is set on advancing side (AS) and the aluminum is set on retreating side (RS) [26]. In the welding process, welding direction is along the length of workpiece and the workpiece traverse speed is the controlled variable. In order to select appropriate

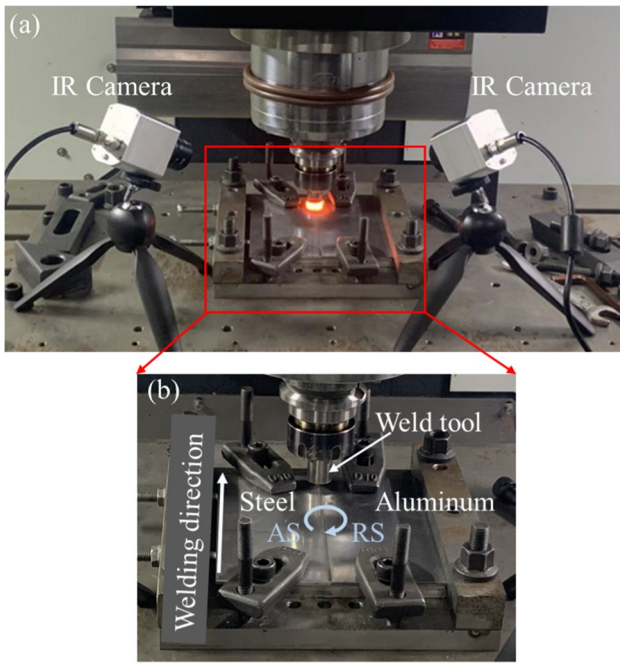


**Fig. 1** The FSW equipment for aluminum-steel joint. **a** The system included IR camera to measure the temperature. **b** Magnified views of workpiece and clamp in **a**

**Table 1** FSW process parameters of test cases

Test case	Traverse speed (mm/min)	Rotated speed (r/min)	Tool offset (mm)
1#	40	800	0
2#	50	800	0
3#	60	800	0
4#	70	800	0
5#	80	800	0

process parameters, pre-experiments with rotational speed of 600 rpm, 700 rpm, and 800 rpm were performed. Then the welding parameters are designed in Table 1.

The specimens for examination of the cross-sectional macrostructure were grounded, polished, and etched with different solution due to dissimilar material. Firstly, 304 stainless steel was etched with concentrated aqua regia solution (30 mL hydrochloric acid and 10 mL nitric acid) for 15 s and then 6061 aluminum alloy was etched with Keller’s solution (95 mL water, 1.5 mL hydrochloric acid, 2.5 mL nitric acid, 1 ml hydrofluoric acid) for 60 s. After that, the cross-sectional macrostructure and microstructure of specimens was observed by optical microscopy and scanning electron microscopy.

### 3 Numerical model

#### 3.1 Assumptions

The following simplifying assumptions are made to make the heat transfer numerical calculations between weld tool and workpiece tractable.

- (1) Comparing with fusion weld, the temperature is below the melting point during FSW, so the material thermo-physical parameters are assumed to be constant, but the viscosity of the material varied with temperature.
- (2) The FSW process is assumed to be quasi-steady state, while the transient process at the beginning and end of welding are ignored.

#### 3.2 Governing equations

The conservation equations of mass, momentum and energy were solved, using the commercial package, ANSYS Fluent [27]. The steady-state continuity equation, momentum conservation equations, and energy equation for incompressible multi-phase flow were given by [28]:

$$\nabla \cdot (\bar{\rho}\vec{v}) = 0 \tag{1}$$

$$\nabla \cdot (\bar{\rho} \vec{v} \vec{v}) = -\nabla p + \nabla \cdot (\bar{\mu}\nabla\vec{v}) - \nabla \cdot (\bar{\rho} \vec{U} \vec{v}) \tag{2}$$

$$\nabla \cdot (\bar{\rho} \vec{v} H) = \nabla \cdot \left( \frac{\bar{k}}{\bar{C}_p} \nabla H \right) - \nabla \cdot (\bar{\rho} \vec{U} H) + S_v \tag{3}$$

$$\bar{\rho} = \sum_{i=1}^2 \Omega_i \rho_i \tag{4}$$

$$\bar{\mu} = \sum_{i=1}^2 \Omega_i \mu_i \tag{5}$$

$$\bar{k} = \sum_{i=1}^2 \Omega_i k_i \tag{6}$$

$$\bar{C}_p = \sum_{i=1}^2 \Omega_i C_{pi} \tag{7}$$

where  $\bar{\rho}$  is the mix density,  $\bar{\mu}$  is the mix non-Newtonian viscosity,  $p$  is the pressure,  $\vec{v}$  is the velocity of material flow,  $\vec{U}$  is the welding velocity,  $H$  is the total enthalpy of the material,  $\bar{k}$  is the mix thermal conductivity and  $\bar{C}_p$  is the mix specific heat.  $S_v$  is the viscous dissipation heat generation

due to plastic material flow originated by high strain rate inside the shear zone of the workpiece near the tool.  $\Omega_i$  is the volume fraction of each phase.  $\rho_i$  is the density of  $i$  phase.  $\mu_i$  is the non-Newtonian viscosity of  $i$  phase.  $k_i$  is the thermal conductivity of  $i$  phase.  $C_{p_i}$  is the specific heat of  $i$  phase.

### 3.3 Calculation zones and boundary conditions

Considering the weld tool and dissimilar properties of 6061 aluminum alloy and 304 stainless steel, the calculation zones should be set carefully. In this study, the whole domain is divided into four calculation zones including steel zone, aluminum zone, weld tool head zone, and weld tool pin zone as shown in Fig. 2.

Nigh kinds of boundaries corresponding with each calculation zone are listed in Table 2. In this model, material flows into and out the computational domain through the ‘inlet’ and ‘outlet’ boundary with same traverse speed in the experiment. The translational momentum boundary indicates the surface moves with same speed corresponding to the weld parameters list in Table 1, so as well as the rotational momentum

boundary. In terms to the thermal boundary conditions, the type of ‘Inlet’ and ‘Outlet’ is temperature which equal to the ambient temperature 300 K. The heat transfer is convection at the ‘top surface’, ‘back surface’, and ‘side surface’, the corresponding heat transfer coefficient are estimated as 30 W/m<sup>2</sup>-K [29], 800 W/m<sup>2</sup>-K [30], and 800 W/m<sup>2</sup>-K [30] respectively. Frictional heat will be generated on the ‘shoulder interface’, ‘pin interface’, and ‘pin bottom’ boundaries, the calculation equations will be given in the section of heat generation. No heat generation is assumed at the ‘tool head side’ boundary, so the heat flux is set as 0 W/m<sup>2</sup>.

Figure 3 shows the mesh of the geometry model. The model contains 128,667 mixed cells of steel zone, 128,673 mixed cells of aluminum zone, 4600 hexahedral cells of weld tool head zone, and 468 hexahedral cells of weld tool pin zone. In order to obtain the accurate distribution of heat flux and reduce the calculation time, a smaller mesh size is applied in the vicinity of the welding tool and the mesh size gradually increases with increasement of the radial distance. The maximum and minimum volume of hexahedral cells in the model are  $2.21 \times 10^{-9} \text{ m}^3$  and  $1.82 \times 10^{-11} \text{ m}^3$  respectively.

**Fig. 2** Schematic of the calculation zones and boundary positions consisting of weld tool and workpiece

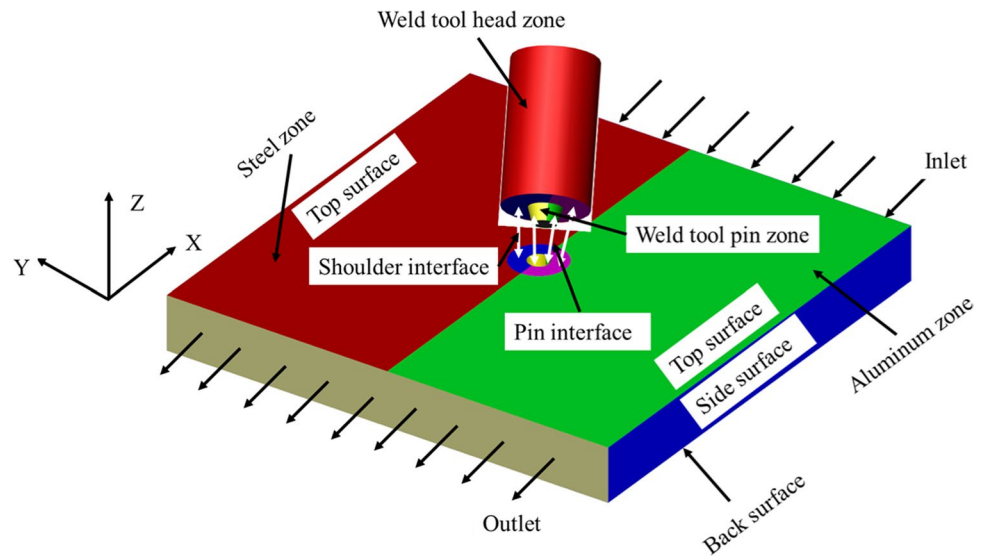


**Table 2** Boundary conditions in the models

Boundary	Type	Momentum	Thermal
Inlet	Velocity inlet	Translational	Temperature (300 K)
Outlet	Velocity outlet	Translational	Temperature (300 K)
Top surface	Wall (no slip)	Translational	Convection (30 W/m <sup>2</sup> -K)
Back surface	Wall (no slip)	Translational	Convection (800 W/m <sup>2</sup> -K)
Side surface	Wall (no slip)	Translational	Convection (800 W/m <sup>2</sup> -K)
Shoulder interface	Wall (no slip)	Rotational	Coupled (heat generation)
Pin interface	Wall (no slip)	Rotational	Coupled (heat generation)
Pin bottom	Wall (no slip)	Rotational	Coupled (heat generation)
Tool head side	Wall (no slip)	Rotational	Heat flux (0 W/m <sup>2</sup> )

**Fig. 3** The mesh of aluminum-steel joint and weld tool

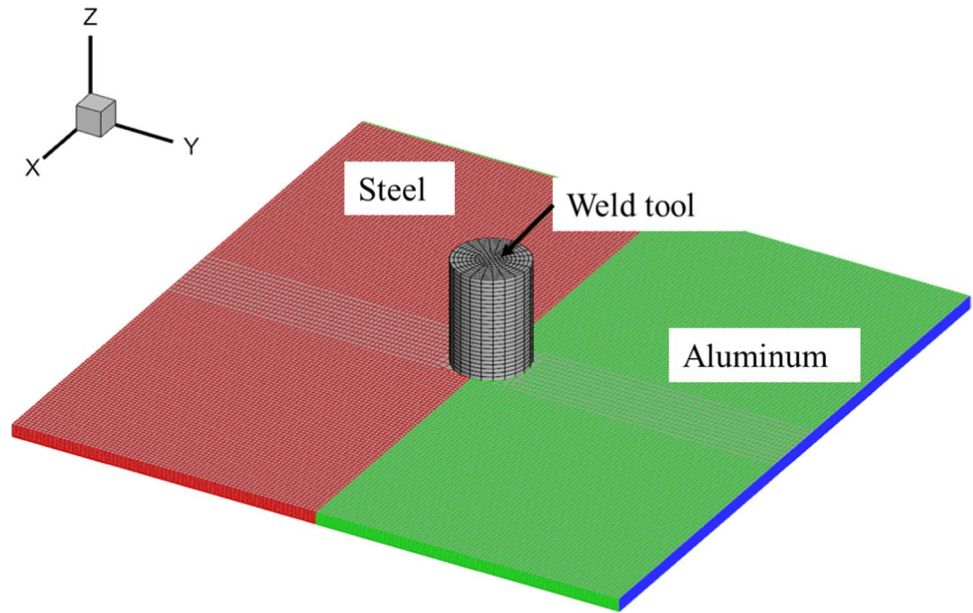


**Table 3** Thermophysical parameters of 304 stainless steel, 6061 aluminum alloy and H13 steel [31, 32]

Properties	304	6061	H13
Density (kg/m <sup>3</sup> )	7800	2705	7800
Specific heat (J/kg-K)	520	850	734.3
Thermal conductivity (W/m-K)	24	210	30.4

### 3.4 Material thermophysical parameters

The materials of joint and weld tool are dissimilar material, so the thermophysical parameters should be loaded to the corresponding calculation zone. The thermophysical parameters of the alloys are provided in Table 3 [31, 32].

The viscosity is important for material flow and heat generation, so it is determined by the below formula based on the theory of visco-plasticity [33]:

$$\mu = \frac{\sigma}{3\dot{\epsilon}} \tag{8}$$

where  $\sigma$  is flow stress of the workpiece and  $\dot{\epsilon}$  is the effective strain rate, which is defined by

$$\dot{\epsilon} = \sqrt{\frac{2}{3} \dot{\epsilon}_{ij} \dot{\epsilon}_{ij}} \tag{9}$$

where  $\dot{\epsilon}_{ij}$  is the strain rate tensor given by

$$\dot{\epsilon}_{ij} = \frac{1}{2} \left( \frac{\partial v_i}{\partial x_j} + \frac{\partial v_j}{\partial x_i} \right) \tag{10}$$

The detail calculation of strain rate can be found in Appendix A of reference [34].

Flow stress of the workpiece is considered to be temperature and strain rate dependent and can be obtained through formula (7–8) [35]:

$$\sigma = \frac{1}{\alpha} \ln \left\{ \left( \frac{Z}{A} \right)^{1/n} + \left[ 1 + \left( \frac{Z}{A} \right)^{2/n} \right]^{1/2} \right\} \tag{11}$$

$$Z = \dot{\epsilon} \exp \left( \frac{Q}{RT} \right) \tag{12}$$

where  $T$  is temperature obtained from energy Eq. (3),  $A$  (s<sup>-1</sup>) and  $n$  are material constants,  $Q$  is the thermal deformation activation energy,  $R$  is the ideal gas constant. These parameters can be found in the Table 3 of literature [36].

### 3.5 Heat generation

The heat generation during FSW is consists of plastic deformation and the friction at the welding tool/workpiece interface. The plastic deformation heat is taken into source item  $S_v$  in energy Eq. (3), which is defined by

$$S_v = K \cdot \sigma \cdot \dot{\epsilon} \tag{13}$$

where  $K=0.6$  [3] is the mechanical efficiency.

The heat generated at the welding tool/workpiece interface is set in the boundary conditions. The interfacial friction heat is given as follows:

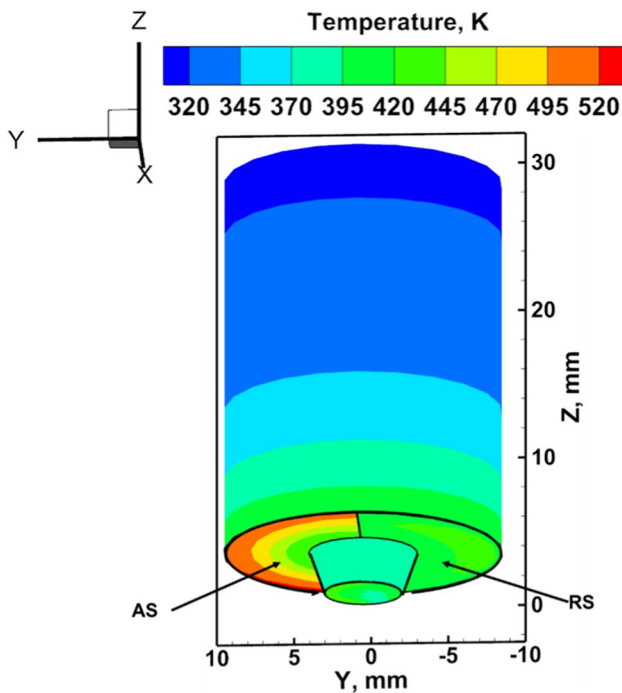


Fig. 4 The temperature field in the weld tool at traverse speed 40 mm/min

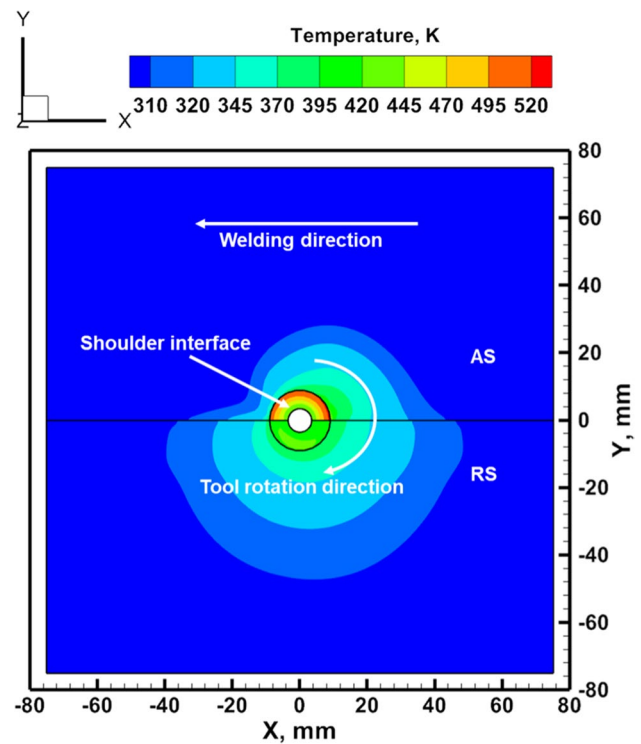


Fig. 5 The temperature field in the workpiece at traverse speed 40 mm/min

$$q_f = \eta \|\vec{\tau}_f\| \|\vec{V}_{vel}\| \tag{14}$$

where  $\eta$  is the ratio of the heat absorbed by the workpiece, which is 0.6 for aluminum alloy and 0.4 for stainless steel;  $\vec{\tau}_f$  is the frictional tangential force and  $\vec{V}_{vel}$  is the relative velocity between the welding tool and the workpiece. The magnitude of these vectors can be calculated from the reference [37]. It should be note that the thermal boundary condition type of the tool/workpiece interface is couple, which assumed heat continuously transfer between the different calculation zones through a very thin wall. The thickness of thin wall in this study is set as 0.01 mm, and the heat generation rate is given as follows:

$$Q_f = \frac{q_f}{a} \tag{15}$$

where  $Q_f$  (W/m<sup>3</sup>) is the heat generation rate at the welding tool/workpiece interface,  $a$  (m) is the thickness of thin wall.

## 4 Results and discussion

### 4.1 Predicted the temperature and material flow

Figure 4 shows the asymmetric temperature field due to the different thermophysical properties of dissimilar materials at the shoulder interface. Because stainless steel at AS has

much lower thermal conductivity, the temperature significantly decreases with radius, which indicates larger inhomogeneity of temperature field at AS. In contrast, the aluminum

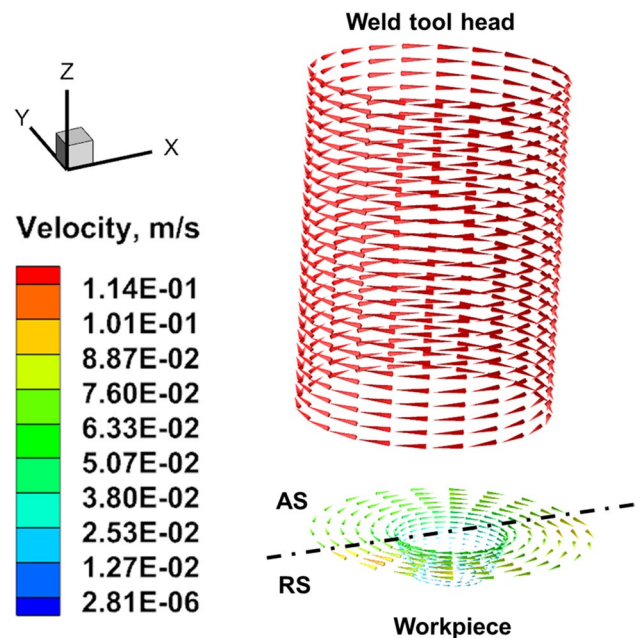
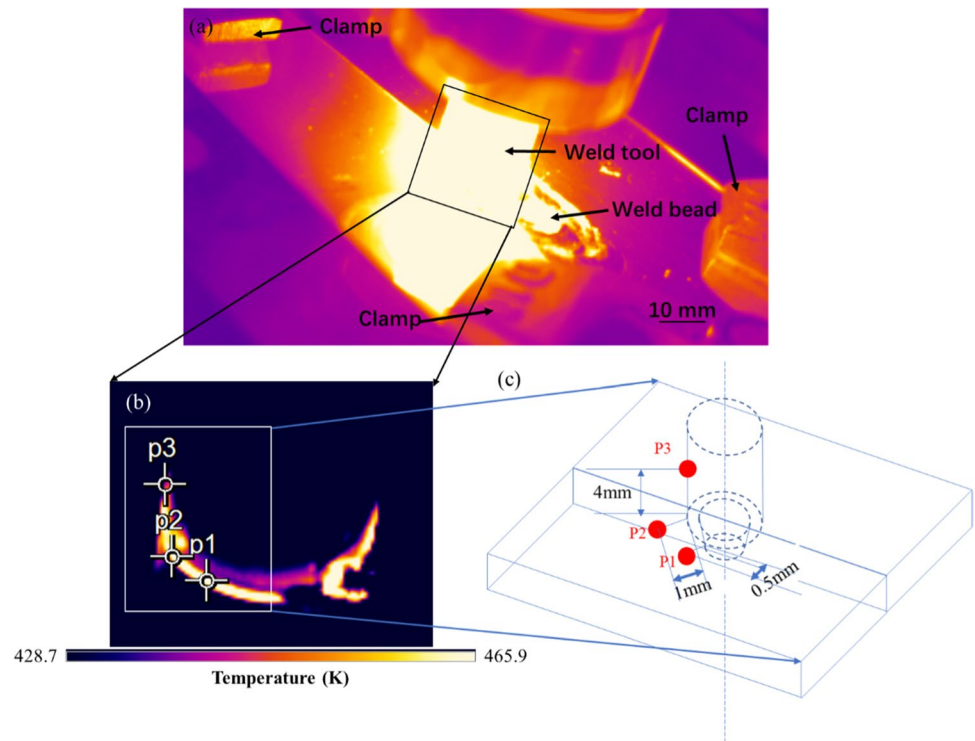


Fig. 6 The material flow in the weld tool and workpiece at traverse speed 40 mm/min

**Fig. 7** **a** The measured temperature field of test case 1. **b** Three points ‘p1’, ‘p2’, and ‘p3’ are selected to validate the model by comparing calculated results and measured results. **c** The distance of measured points in the workpiece and weld tool



alloy has higher thermal conductivity, so the smaller inhomogeneity of temperature field at RS is observed. Similarly, the peak temperature of AS is above 520 K, which is about 100 K higher than that of RS. The inhomogeneity of temperature field at pin interface is not so significant. The temperature of weld tool head decreases with increasing length along Z direction.

Figure 5 shows the temperature field in the workpiece. It is found that the temperature field is corresponded with weld tool due to the coupled boundary condition at the shoulder interface. This indicates that the thickness of thin wall assumption works in the Eq. (15). In the workpiece, it is observed that the temperature field diffused at different velocity, which is measured by diffusion coefficient  $\lambda$  shown as below.

$$\lambda = \frac{k}{C_p} \tag{16}$$

Substituting the thermal conductivity and specific heat of stainless steel and aluminum alloy in the Table 3, the thermal diffusion coefficient of stainless steel is 0.046

**Table 4** Comparisons results between measured and calculated temperature of three monitor points along the weld tool

Points	Measured temperature (K)	Calculated temperature (K)	Relative error
p1	492.3	446.2	9.4%
p2	475.1	435.6	8.3%
p3	439.4	406.3	7.5%

and aluminum alloy is 0.247. The diffusion coefficient of aluminum alloy is about 5 times of stainless steel, so the diffusion width of the temperature field on the RS is much larger.

Figure 6 shows the material flow in the weld tool head and workpiece. The weld tool head rotates without the influence of the workpiece, so it has the maximum velocity, which is same with rotated speed. Near the tool/workpiece interface, the material flows slower than the weld tool. The material flows slightly faster in RS due to the lower viscosity of plastic aluminum alloy.

### 4.2 Validation the temperature filed of aluminum-steel joint

The temperature during FSW process is measured by IR camera. Figure 7 shows the measured temperature field of test case 1, three points in the workpiece and weld tool head are selected to validate the calculation accuracy of the model. The locations of measured points are quantitative by distance from the reference lines as shown in Fig. 7c, so the temperature can be capture in experiments and numerical model.

The calculation temperature and relative error are list in Table 4. It is found that the temperature decreases along upward direction in weld tool, which is consistent with simulation result. The relative error is smaller than 10%, which indicates that the calculation accuracy is accepted. The relative error is higher near the shoulder interface due to the complex thermo-mechanical processes.

**Fig. 8** Microstructures of aluminum-steel joint for the different traverse speed. **a** Traverse speed 60 mm/min. **b** Traverse speed 80 mm/min. **c** SEM analysis of interface zone from **a**. **d** SEM analysis of interface zone from **b**

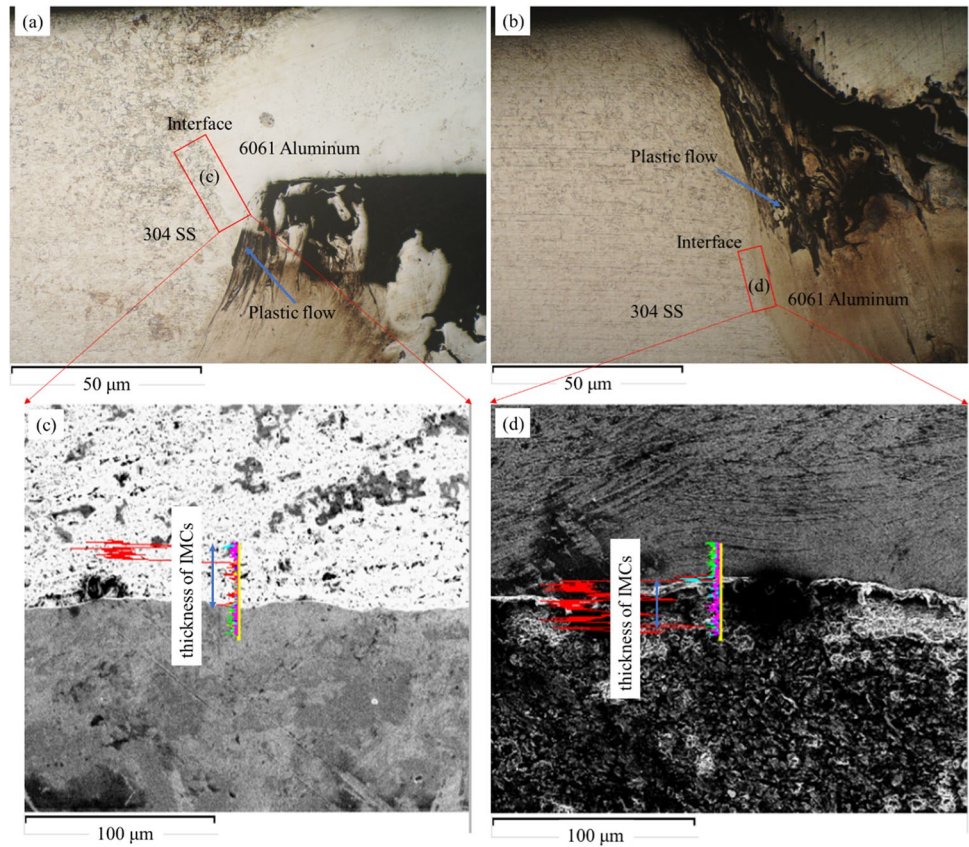
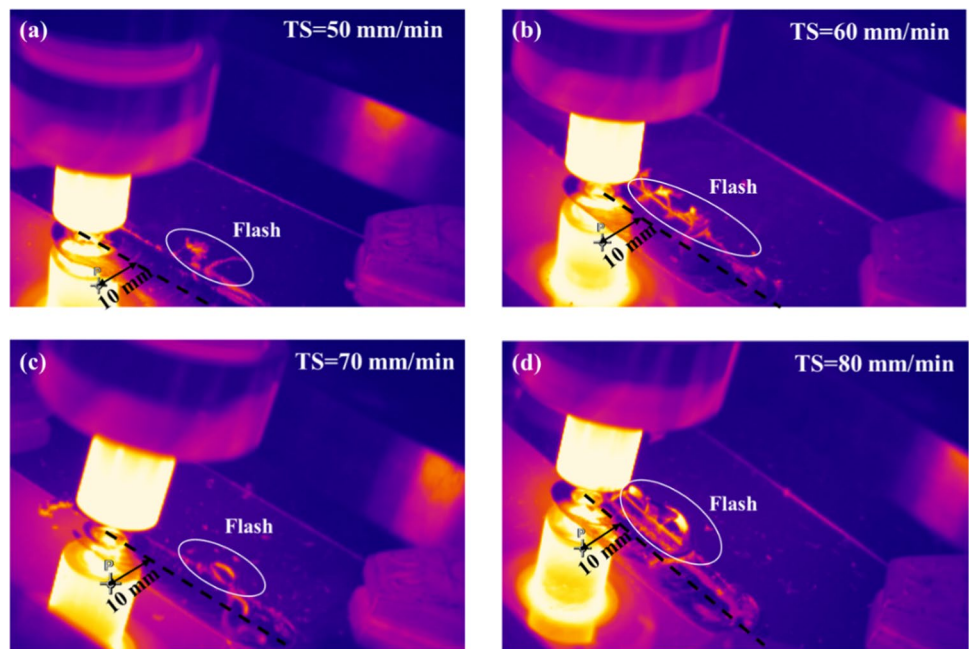


**Fig. 9** The measured temperature field distribution during FSW by the IR camera. ‘TS’ means the different traverse speed. **a** At traverse speed 50 mm/min, **b** at traverse speed 60 mm/min, **c** at traverse speed 70 mm/min, **d** at traverse speed 80 mm/min

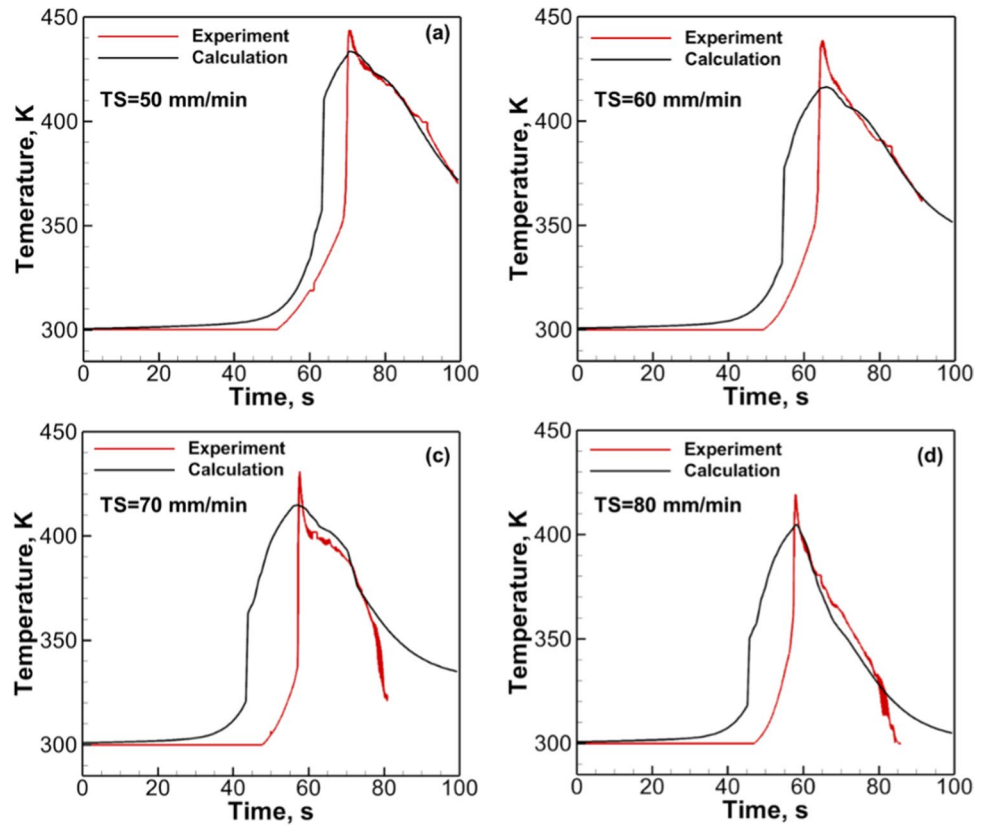


The thermal cycle curve plays an important role in determining weld joint microstructure, properties, and performance. According to Zener-Hollomon equation related to the temperature and strain rate during different weld process, Bagheri et al. [38] found that the weld region grains for

FSVW were finer compared with those for FSW of AA6061-T6 joints. Abdollahzadeh et al. [39] found that a refined microstructure in the stir zone can be observed by performing underwater friction stir welding, which significantly decreased the joint temperature of AA6061-T6 alloys. In this study, the



**Fig. 10** Comparison between the calculated and the experimentally measured thermal cycles at different traverse speed. **a** At traverse speed 50 mm/min, **b** at traverse speed 60 mm/min, **c** at traverse speed 70 mm/min, **d** at traverse speed 80 mm/min



peak temperature and cooling rate is controlled by the traverse speed. The microstructure evolution of aluminum-steel joint at different traverse speed is shown in Fig. 8. The grains in 304 stainless steel side were finer and the plastic flow was stronger at 80 mm/min traverse speed compared with those at 60 mm/min traverse speed. The reason may be that the stronger plastic flow at 80 mm/min traverse speed led to the lower peak temperature, according to Zener-Hollomon equation, the grain is finer. The stronger plastic flow at 80 mm/min traverse speed also led to faster cooling rate, it may cause the thinner thickness of IMCs at the interface between aluminum and steel, as shown in Fig. 8c, d.

Figure 9 shows the measured points at different traverse speed are captured by IR camera. Because the relative error near the shoulder interface is higher, the measured point is set as 10 mm distance from the joint center. At the end of FSW, the temperature of weld tool is higher than the workpiece and the flash is also observed. Although, the temperature of flash can be measured by IR camera, it cannot be considered in this model. This is one of the error sources of thermal cycle calculation.

Since the quasi-steady state assumption is adopted in this model, the thermal cycle can be calculated based on the Eq. (16) in reference [40]. The comparison results between experiment and calculation are shown in Fig. 10. The peak temperature can be extracted from thermal cycle curve and presented in Table 5.

Based on data in Table 5, the calculation peak temperature is slightly lower than experiment at corresponding traverse speed. However, the calculation peak temperature is much higher in the model without weld tool. For test case 3, the calculation peak temperature can be 490.4 K and the relative error can be 11.4%. The heating rate of calculation thermal cycle is slightly delay during heat stage. The cooling rate of calculation is better matching with experiments. It seems that the relative error of cooling stage increases with traverse speed. The agreement of the calculated temperature at measured points (Table 4), as well as agreement of thermal cycles for various traverse speed (Fig. 10) with corresponding experimental data provides confidence in using the model to investigate the effects of weld tool on temperature field.

**Table 5** Comparisons results between measured and calculated peak temperature of different traverse speed

Traverse speed (mm/min)	Measured peak temperature (K)	Calculated peak temperature (K)	Relative error
40	452.3	444.5	1.7%
50	445.1	438.8	1.4%
60	440.4	430.1	2.3%
70	434.2	425.6	2.0%
80	425.9	418.2	1.8%

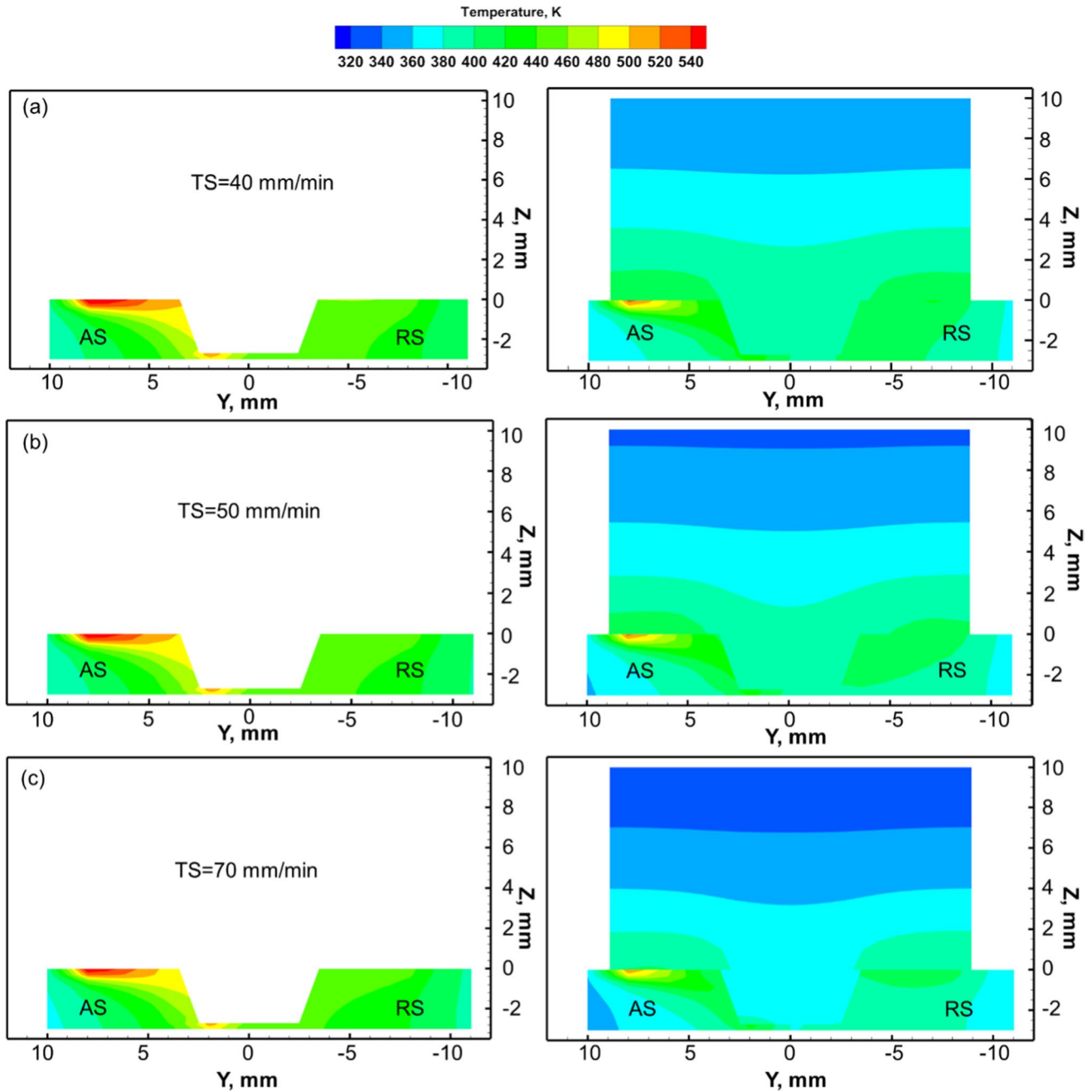


**Fig. 11** Comparison temperature field on YZ cross sections between the model without weld tool and the model with weld tool at the corresponding traverse speed. **a** At traverse speed 40 mm/min, **b** at traverse speed, 50 mm/min, **c** at traverse speed 70 mm/min

### 4.3 Comparison analysis of the effects of welding tool

Figure 11 shows the comparison results of YZ cross sections between the model without weld tool and the model with weld tool. The temperature in AS and RS is quite different due to the dissimilar material. Because much more heat will transfer in the weld tool, it is obviously observed that

much less heat accumulated at AS in the model with weld tool. As the traverse speed increases, the temperature obviously decreases in the model with weld tool, but it slightly decreases in the model without weld tool. It indicates that the model with weld tool fits the experiment results better.

Figure 12 shows the comparison results of XY cross sections between the model without weld tool and the model with weld tool. It is observed that the higher temperature

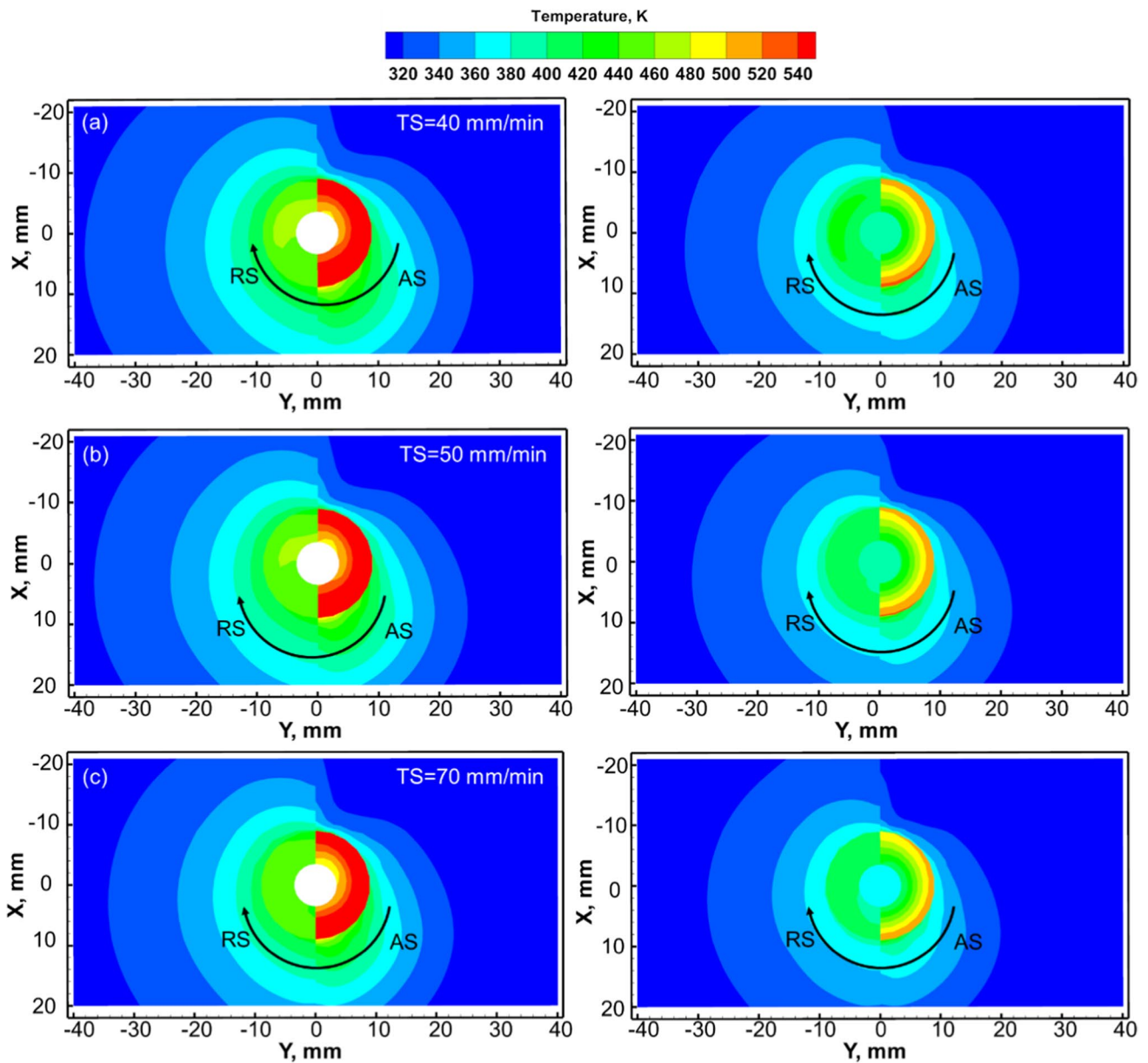


**Fig. 12** Comparison temperature field on XY cross sections between the model without weld tool and the model with weld tool at the corresponding traverse speed. **a** At traverse speed 40 mm/min, **b** at traverse speed 50 mm/min, **c** at traverse speed 70 mm/min

zone is larger at AS in the model without weld tool. In contrasts, the temperature gradient is lower in the model with weld tool. This is because the weld tool can also transfer heat, it reduces the temperature difference between AS and RS. The maximum temperature difference between AS and RS can be above 200 K in the model without weld tool, but this temperature difference is about 150 K in the model with weld tool. It indicates that the smaller inhomogeneity of temperature field is obtained by employing the model with weld tool.

The temperature gradient is also different between AS and RS due to the dissimilar aluminum-steel joint. Figure 13 shows the temperature gradient varied with traverse speed at AS and RS. If the traverse speed is same, the temperature gradient is about 30 K/mm larger at AS than that at RS. In additions, the temperature gradient is about 20 K/mm larger at AS and 5 K/mm larger at RS in the model without weld tool. As the traverse speed increases, the temperature gradient both decreases in the model without weld tool and the model with weld tool.

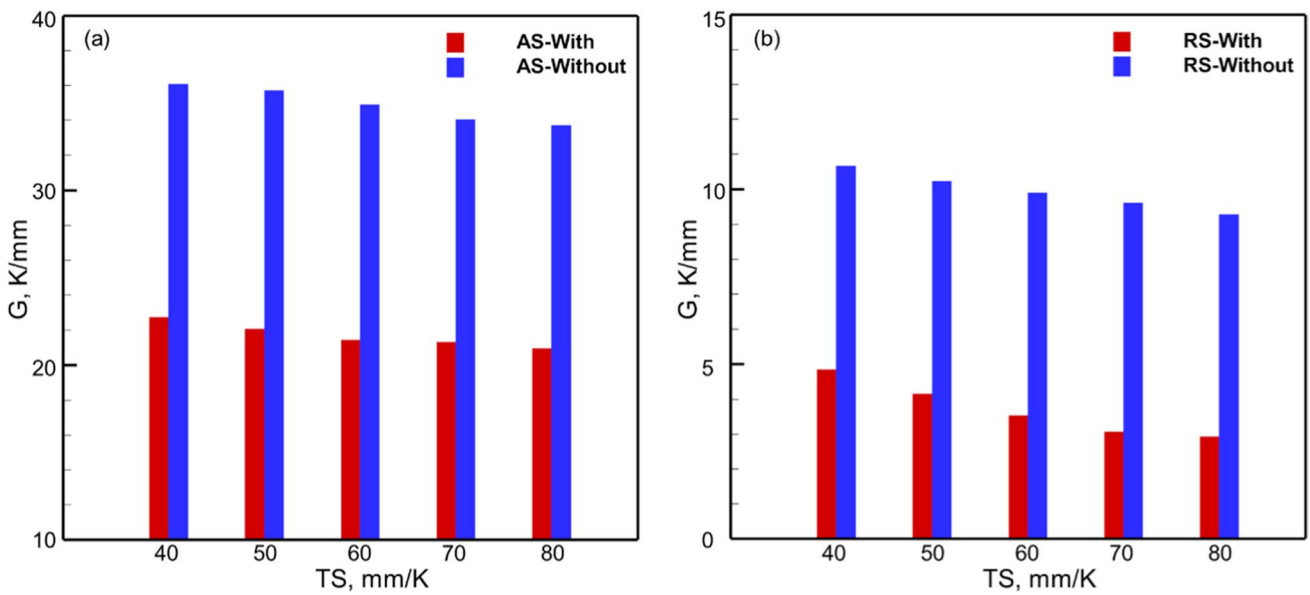


**Fig. 13** Temperature gradient varied with traverse speed between the model without weld tool and the model with weld tool. **a** At AS, where ‘AS-With’ means the model with weld tool at AS, ‘AS-Without’ means the model without weld tool, **b** at RS, where ‘RS-

With’ means the model with weld tool at RS, ‘RS-Without’ means the model without weld tool. ‘TS’ indicates traverse speed and ‘G’ indicates the temperature gradient

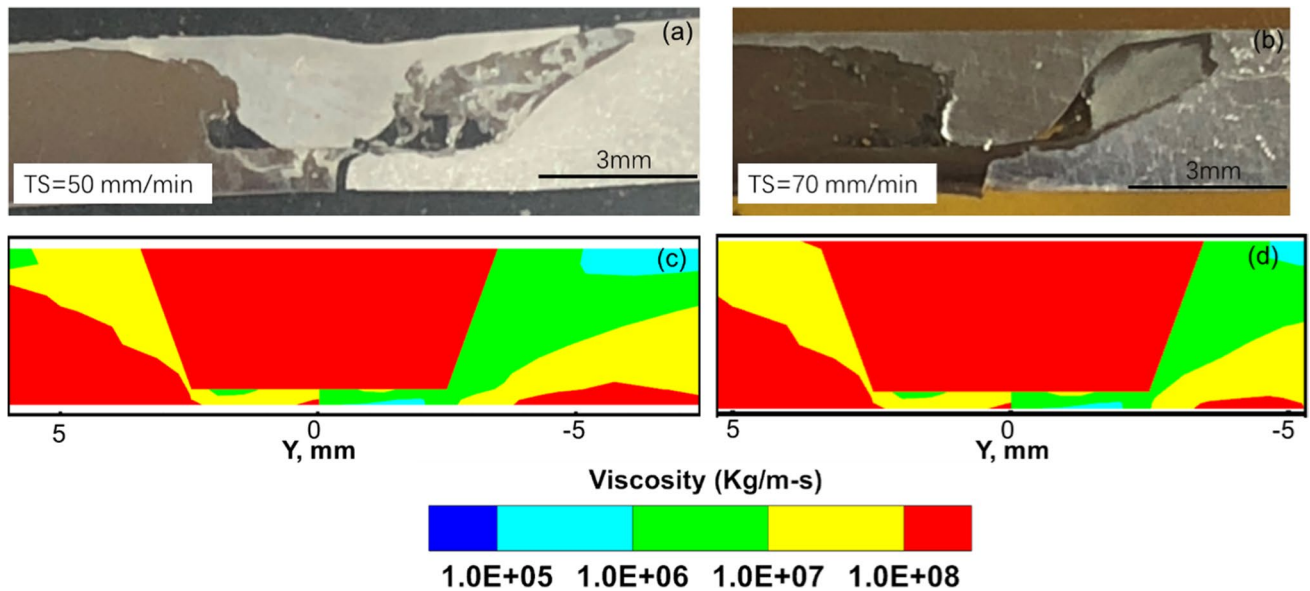


**Fig. 14** The macrostructure of aluminum-steel joint at corresponding traverse speed **a** 50 mm/min, **b** 70 mm/min. The calculated viscosity near the pin at corresponding traverse speed, **c** 50 mm/min, **d** 70 mm/min

The large temperature difference and temperature gradient at AS and RS determine the relationship between macrostructure and viscosity. Figure 14 shows the macrostructure and viscosity near the pin at two different traverse speed level. It is observed that the material is

insufficient stirring at RS due to the different material viscosity. Although this kind of defect cannot be simulated in this model, the model can provide calculated viscosity based on the temperature field as shown in Fig. 11. Since the significant inhomogeneity of temperature field

for aluminum-steel joint, the steel and aluminum viscosity can differ by an order of magnitude. As the traverse speed increases, the peak temperature and temperature difference between AS and RS decreased, so the plastic zones shrink at 70 mm/min traverse speed as shown in Fig. 14d.

## 5 Conclusions

In this paper, a novel CFD model with weld tool is developed to investigate the effects of weld tool on the aluminum-steel joint. The following conclusions could be obtained:

- (1) The calculated temperature and thermal cycles for various traverse speed agreed well with the corresponding IR experimental results. The relative error of monitor points is smaller than 10%, which indicates that the calculation accuracy is accepted.
- (2) The model with weld tool can decrease the relative error of peak temperature. Based on Table 5, the calculated peak temperature is about 10 K lower than measured peak temperature and the relative error is 2.3%, while it is 11.4% for the model without weld tool.
- (3) The model with weld tool decreases the temperature gradient for aluminum-steel joint to provide the more accurate prediction results. The calculated temperature gradient with weld tool is about 20 K/mm lower at AS and 5 K/mm lower at RS than those in the model without weld tool.
- (4) The model with weld tool decreases the inhomogeneity of temperature field. The maximum temperature difference between AS and RS can be above 200 K in the model without weld tool, but this temperature difference is about 150 K in the model with weld tool.
- (5) SEM analysis of the interface between aluminum and steel showed that the thickness of IMCs may decrease with traverse speed. The model with weld tool can provide calculated viscosity based on temperature field to analyze the insufficient stirring defect.

**Authors' contributions** Wenmin Ou and Guolin Guo conceived and designed the study. Chenshuo Cui and Yaocheng Zhang performed the experiments. Longgen Qian and Wenin Ou established the model. Wenmin Ou and Guolin Guo reviewed and edited the manuscript. All the authors read and approved the final manuscript.

**Funding** This work was supported by the Natural Science Fund for Colleges and Universities in Jiangsu Province (20KJB460013).

**Data availability** The datasets generated and/or analyzed during the current study are available from the corresponding author on reasonable request.

**Code availability** The codes used to reproduce this work cannot be shared at this time as they are part of an ongoing study.

## Declarations

**Ethics approval** Not applicable.

**Consent to participate** Not applicable.

**Consent for publication** The author confirms that the work has not been published before; that it is not under consideration for publication elsewhere that its publication has been approved by all co-authors; that its publication has been approved by the responsible authorities at the institution where the work is carried out.

**Competing interests** The authors declare that they have no competing interests.

## References

1. Taban E, Gould JE, Lippold JC (2010) Dissimilar friction welding of 6061-T6 aluminum and AISI 1018 steel: properties and microstructural characterization. *Mater Des* 31(5):2305–2311
2. Hussein SA, Md Tahir AS, Hadzley AB (2015) Characteristics of aluminum-to-steel joint made by friction stir welding: a review. *Mater Today Commun* 5:32–49
3. Heidarzadeh A, Mironov S, Kaibyshev R et al (2021) Friction stir welding/processing of metals and alloys: a comprehensive review on microstructural evolution. *Prog Mater Sci* 117:100752
4. Bagheri B, Abbasi M, Sharifi F, Abdollahzadeh A (2022) Investigation into novel multipass friction stir vibration brazing of carbon steels. *Mater Manuf Process* 37(8):921–932
5. Bagheri B, Abbasi M, Sharifi F, Abdollahzadeh A (2022) Different attempt to improve friction stir brazing: effect of mechanical vibration and rotational speed. *Met Mater Int* 28:2239–2251
6. Bozzi S, Helbert-Etter AL, Baudin T, Criqui B, Kerbiguetc JG (2010) Intermetallic compounds in Al 6016/IF-steel friction stir spot welds. *Mater Sci Eng, A* 527(16–17):4505–4509
7. Wan L, Huang Y (2018) Friction stir welding of dissimilar aluminum alloys and steels: a review. *Int J Adv Manuf Technol* 99(5):1781–1811
8. Derazkola HA, Khodabakhshi F (2019) Intermetallic compounds (IMCs) formation during dissimilar friction-stir welding of AA5005 aluminum alloy to St-52 steel: numerical modeling and experimental study. *Int J Adv Manuf Technol* 100(9):2401–2422
9. Xiong JT, Li JL, Qian JW, Zhang FS, Huang WD (2012) High strength lap joint of aluminium and stainless steels fabricated by friction stir welding with cutting pin. *Sci Technol Weld Joining* 17(3):196–201
10. Wang TH, Sidhar H, Mishra RS, Hovanski Y, Upadhyay P, Carlson B (2018) Friction stir scribe welding technique for dissimilar joining of aluminium and galvanised steel. *Sci Technol Weld Joining* 23(3):249–255
11. Patterson EE, Hovanski Y, Field DP (2016) Microstructural characterization of friction stir welded aluminum-steel joints. *Metall Mater Trans A* 47(6):2815–2829
12. Nandan R, Debroy T, Bhadeshia HKDH (2008) Recent advances in friction-stir welding – process, weldment structure and properties. *Prog Mater Sci* 53(6):980–1023
13. He XC, Gu FS, Ball A (2014) A Review of Numerical Analysis of Friction Stir Welding. *Prog Mater Sci* 65(10):1–66
14. Su H, Wu CS, Bachmann M, Rethmeier M (2015) Numerical modeling for the effect of pin profiles on thermal and material flow characteristics in friction stir welding. *Mater Des* 77(15):114–125

15. Bagheri B, Abdollahzadeh A, Abbasi M, Kokabi AH (2020) Numerical analysis of vibration effect on friction stir welding by smoothed particle hydrodynamics (SPH). *Int J Adv Manuf Technol* 110:209–228
16. Bagheri B, Abbasi M, Abdollahzadeh A, Kokabi AH (2020) Numerical analysis of cooling and joining speed effects on friction stir welding by smoothed particle hydrodynamics (SPH). *Arch Appl Mech* 90:2275–2296
17. Sun Z, Wu CS (2020) Influence of tool thread pitch on material flow and thermal process in friction stir welding. *J Mater Process Technol* 275:116281
18. Chen GQ, Li H, Wang GQ et al (2018) Effects of pin thread on the in-process material flow behavior during friction stir welding: a computational fluid dynamics study. *Int J Mach Tools Manuf* 124:12–21
19. Chen GQ, Ma QX, Zhang S et al (2018) Computational fluid dynamics simulation of friction stir welding: a comparative study on different frictional boundary conditions. *J Mater Sci Technol* 34(1):128–134
20. Aziz SB, Dewan MW, Huggett DJ et al (2018) A fully coupled thermomechanical model of friction stir welding (FSW) and numerical studies on process parameters of lightweight aluminum alloy joints. *Acta Metall Sinica-English Lett* 31:1–18
21. Dialami N, Chiumenti M, Cervera M et al (2017) Enhanced friction model for friction stir welding (FSW) analysis: simulation and experimental validation. *Int J Mech Sci* 133:555–567
22. Chen GQ, Wang GQ, Shi QY et al (2019) Three-dimensional thermal-mechanical analysis of retractable pin tool friction stir welding process. *J Manuf Process* 41:1–9
23. Aziz SB, Dewan MW, Huggett DJ et al (2016) Impact of friction stir welding (FSW) process parameters on thermal modeling and heat generation of aluminum alloy joints. *Acta Metall Sinica-English Lett* 29(9):1–15
24. Miles MP, Nelson TW, Gunter C et al (2019) Predicting recrystallized grain size in friction stir processed 304L stainless steel. *J Mater Sci Technol* 35(4):491–498
25. Mirabzadeh R, Parvaneh V, Ehsani A (2021) Experimental and numerical investigation of the generated heat in polypropylene sheet joints using friction stir welding (FSW). *Int J Mater Form* 14:1067–1083
26. Lee WB, Schmuecker M, Mercardo UA et al (2006) Interfacial reaction in steel–aluminum joints made by friction stir welding. *Scripta Mater* 55(4):255–358
27. FLUENT, Release 2019 R3 - © ANSYS, Inc. All rights reserved
28. Derazkola HA, Eyvazian A, Simchi A (2020) Submerged friction stir welding of dissimilar joints between an Al-Mg alloy and low carbon steel: Thermo-mechanical modeling, microstructural features, and mechanical properties. *J Manuf Process* 50:68–79
29. Yu ZZ, Zhang W, Choo H et al (2012) Transient heat and material flow modeling of friction stir processing of magnesium alloy using threaded tool. *Metall and Mater Trans A* 43:724–737
30. Chen GQ, Shi QY, Li YJ et al (2013) Computational fluid dynamics studies on heat generation during friction stir welding of aluminum alloy. *Comput Mater Sci* 79:540–546
31. Mills KC (2002) Recommended values of thermophysical properties for selected commercial alloys, Woodhead Publishing, pp 61–65 127–128
32. Ou W, Mukherjee T, Knapp GL et al (2018) Fusion zone geometries, cooling rates and solidification parameters during wire arc additive manufacturing. *Int J Heat Mass Transf* 127:1084–1094
33. Colegrove PA, Shercliff HR (2005) 3-Dimensional CFD modelling of flow round a threaded friction stir welding tool profile. *J Mater Process Technol* 169(2):320–327
34. Nandan R, Roy GG, Debroy T (2006) Numerical simulation of three-dimensional heat transfer and plastic flow during friction stir welding. *Metall Mater Trans A* 37(4):1247–1259
35. Sheppard T, Jackson A (1997) Constitutive equations for use in prediction of flow stress during extrusion of aluminum alloys. *Metal Sci J* 13(3):203–209
36. Tello KE, Gerlich AP, Mendez PF (2010) Constants for hot deformation constitutive models for recent experimental data. *Sci Technol Weld Joining* 15(3):260–266
37. Chen GQ, Feng ZL, Zhu YC et al (2016) An alternative frictional boundary condition for computational fluid dynamics simulation of friction stir welding. *J Mater Eng Perform* 25:4016–4023
38. Bagheri B, Abbasi M, Abdollahzadeh A (2021) Microstructure and mechanical characteristics of AA6061-T6 joints produced by friction stir welding, friction stir vibration welding and tungsten inert gas welding: A comparative study. *Int J Miner Metall Mater* 28:450–461
39. Abdollahzadeh A, Bagheri B, Abassi M et al (2021) Comparison of the Weldability of AA6061-T6 Joint under Different Friction Stir Welding Conditions. *J Mater Eng Perform* 30:1110–1127
40. Mundra K, Debroy T, Kelkar KM (1996) Numerical prediction of fluid flow and heat transfer in welding with a moving heat source. *Numer Heat Transf, Part A: Appl* 29(2):115–129

**Publisher's note** Springer Nature remains neutral with regard to jurisdictional claims in published maps and institutional affiliations.

Springer Nature or its licensor (e.g. a society or other partner) holds exclusive rights to this article under a publishing agreement with the author(s) or other rightsholder(s); author self-archiving of the accepted manuscript version of this article is solely governed by the terms of such publishing agreement and applicable law.